RSC Advances

PAPER

Cite this: *RSC Adv.*, 2015, **5**, 102173

The influence of replacing Se by Te on electronic structure and optical properties of Tl_4PbX_3 (X = Se or Te): experimental and theoretical investigations

A. H. Reshak,*[ab] Z. A. Alahmed,[c] I. E. Barchij,[d] M. Yu. Sabov,[d] K. J. Plucinski,[e] I. V. Kityk[f] and A. O. Fedorchuk[g]

Received 9th October 2015
Accepted 10th November 2015

DOI: 10.1039/c5ra20956k

www.rsc.org/advances

The energy band structure, electronic charge density and optical features of Tl_4PbSe_3 and Tl_4PbTe_3 single crystals were studied within a framework of the recently modified Becke–Johnson potential (mBJ). The earlier experimentally defined atomic positions were additionally optimized by minimizing the forces acting on the atoms using a generalized gradient approximation (PBE–GGA) approach. The performed band structure calculations have shown that the conduction band minimum (CBM) and the valence band maximum (VBM) are located at the Γ point of the first Brillouin zone, resulting in a direct energy band gap equal to about 0.21 eV (PBE–GGA) and 0.32 eV (mBJ) for Tl_4PbSe_3 in comparison to the experimental value (0.34 eV), while for Tl_4PbTe_3, the band gap is equal to 0.10 eV (PBE–GGA) and 0.18 eV (mBJ) compared with the experimental value (0.19 eV). We have established that the mBJ approach succeeds by a large amount in bringing the calculated energy gaps into close agreement with the measured one. The angular momentum projected density of states explores the existence of weak hybridization between the states, defining the degree of covalent bonding. The calculated valence band electronic charge density space distribution confirms the prevailing covalent origin of the chemical bond. The calculated optical dispersion for the principal optical constants shows that these materials exhibit negative uniaxial anisotropy. We have measured the dispersion of the imaginary part of the dielectric susceptibility ε_2 (ω) and evaluated the experimental optical band gaps. The measured ε_2 (ω) dispersion confirms our theoretical evaluations that the substitution of Se by Te causes a band gap reduction.

1. Introduction

The titled chalcogenide crystals Tl_4PbX_3 (X = Se or Te) are considered to be potential candidates for manufacturing opto-acousto- and thermo-electronic devices.[1–3] Recently, considerable attention also has been devoted to the manufacturing of new thermoelectric materials, in particular thallium chalcogenides.[4,5] Therefore, several thallium containing chalcogenide ternary single crystals have been explored. Among them are the Tl–Sn–S,[6–8] Tl–Sn–Se[9–11] and Tl–Sn–Te[11–14] systems. Thallium and tin in their low oxidation state possess a free doublet of electrons, which could have a stereochemical action and define the material transport properties. In the low oxidation state, Tl_4SnX_3 (X = S, Se, Te) type single crystalline ternaries are formed in the relevant systems. All the ternaries are crystallized in the tetragonal 4/*mmm* crystallographic point group. But the symmetry of $Tl_4SnS_3(Se_3)$ is lower (space group *P*4/*nmm*)[15,16] compared to Tl_4SnTe_3 (space group *I*4/*mcm*).[17] The thallium compounds possess some specific features[18] due to the high polarizability of the Tl ions.

However, their further applications are restrained by the absence of reliable electronic parameters which may be obtained from density functional theory (DFT) calculations. Therefore, this fact motivated us to devote more attention to a comprehensive theoretical calculation using the all-electron full potential linear augmented plane wave plus local orbitals (FP − LAPW + lo) method[19] within different exchange correlation potentials (XC), including the recently modified Becke–Johnson potential (mBJ).[21] The latter potential optimizes the corresponding potential for electronic band structure calculations. The modified Becke–Johnson potential allows calculation with accuracy that is similar to very expensive GW calculations.[20] It is a local approximation to an atomic "exact-exchange" potential and a screening term. We have

[a]*New Technologies - Research Centre, University of West Bohemia, Univerzitni 8, 306 14 Pilsen, Czech Republic. E-mail: maalidph@yahoo.co.uk*

[b]*Center of Excellence Geopolymer and Green Technology, School of Material Engineering, University Malaysia Perlis, 01007 Kangar, Perlis, Malaysia*

[c]*Department of Physics and Astronomy, King Saud University, Riyadh 11451, Saudi Arabia*

[d]*Department of Chemistry, Uzhgorod National University, Pidgirna str. 46, 88000, Uzhgorod, Ukraine*

[e]*Electronics Department, Military University Technology, Kaliskiego 2, Warsaw 00-908, Poland*

[f]*Faculty of Electrical Engineering, Czestochowa University Technology, Armii Krajowej 17, PL-42201, Czestochowa, Poland*

[g]*Lviv National University of Veterinary Medicine and Biotechnologies, Pekarska Street 50, 79010 Lviv, Ukraine*

calculated the electronic band structure dispersion, space electronic charge distribution, the total and angular momentum resolved projected density of states and the optical properties for Tl_4PbX_3 (X = Se or Te) single crystals. The investigation of the optical properties clarifies the origin of the electronic band structure. Therefore, we are interested in calculating the optical properties of the investigated compound. The FP − LAPW + lo method has proven to be one of the accurate methods for the computation of the electronic structure of solids within DFT.[21–25]

The dielectric susceptibility dispersion was measured by an ellipsometry method. The surfaces of the samples were polished with roughness values of up to 12.0 mm in the spectral range up to 6.0 eV with a spectral resolution of 0.2 eV.

In ref. 26, we performed initial experimental X-ray diffraction studies of the titled compounds. In order to verify these data, we have performed DFT self-consistent simulations to verify the deviations of the particular atoms from their XRD positions.

2. Experimental part

The ternaries were synthesized from elements of high purity (Tl–99.99 wt%, Sn–99.998 wt%, S–99.999 wt%, Se–99.999 wt%, Te–99.99 wt%). The thallium was covered by a surface oxide, which was removed before use. All syntheses were carried out in previously cleaned and dried quartz tubes with narrow ends. Then, they were vacuum-sealed (0.13 Pa). According to Tl_2X–SnX (X–S, Se, Te) phase diagrams, $Tl_4SnSe_3(Te_3)$ melts congruently, but Tl_4SnS_3 melts incongruently. Given this fact, the $Tl_4SnSe_3(Te_3)$ compounds were synthesized from stoichiometric amounts of components and Tl_4SnS_3 was synthesized from non-stoichiometric contents, which were richer in SnS from the region of primary crystallization of the ternary compound. The samples were heated to the liquid state (673 K for Tl_4SnS_3, 763 for Tl_4SnSe_3 and 873 K for Tl_4SnTe_3) and maintained for 24 hours at maximal temperature. Then, the samples were subjected to cooling until the annealing temperature was reached (453 K for Tl_4SnS_3, 523 for Tl_4SnSe_3 and 583 K for Tl_4SnTe_3) and maintained for 3 days. Then the samples were placed into vertical two zone furnaces. Crystals were grown by the Bridgman method. The temperatures of the zones were stabilized with ±0.5 K accuracy. The solidification rate was 0.1–0.3 mm h^{-1}, and the temperature gradient at the solid–liquid interface was equal to about 2–4 K mm^{-1}. The temperatures of the solidification zone were equal to the annealing temperature. The atomic coordinates for Tl_4PbSe_3 (SG *P*4/*ncc* (130); $a = 8.5346$ (2), $c = 12.6871$ (7) Å)[26] and for Tl_4PbTe_3 (SG *I*4/*mcm* (140); $a = 8.841$, $c = 13.056$ Å)[27] are listed in Tables 1 and 2, in comparison with the optimized coordinates obtained from DFT calculations within the generalized gradient approximation (PBE–GGA).[28]

3. Theoretical part-calculation methodology

It has been reported that Tl_4PbSe_3 and Tl_4PbTe_3 crystallize in a tetragonal structure with the space group *P*4/*ncc* (no. 130) and *I*4/*mcm* (no. 140). The crystalline structures of Tl_4PbSe_3 and Tl_4PbTe_3 are shown in Fig. 1. To investigate the electronic structure of the two compounds, the X-ray diffraction data obtained by our group were used as input data for comprehensive theoretical calculations. The experimental crystal structures were optimized by minimizing the forces acting on each atom, using the all-electron full potential linear augmented plane wave plus local orbitals (FP − LAPW + lo) method, as implemented in the WIEN2k code[19] within the PBE–GGA approach. Generally, the optimized crystal structures are in good agreement with the experimental crystallographic data as listed in Tables 1 and 2. The relaxed geometry was used to calculate the electronic band structure, the angular momentum projected density of states, the electronic charge density distribution and the chemical bonding features using the recently modified Becke–Johnson potential. This potential allows us to perform calculations with accuracy similar to that of very expensive GW calculations.[20] It is a local approximation to an atomic "exact-exchange" potential and a screening term.

A spherical harmonic expansion was used inside non-overlapping spheres of muffin–tin radius (R_{MT}) and the plane wave basis set was chosen in the interstitial region (IR) of the unit cell. The R_{MT} values for Tl, Pb, Se and Te atoms were chosen in such a way that the spheres did not overlap, therefore 2.5 a.u is the best R_{MT} value for the titled crystals. To achieve total energy convergence, the basis functions in the IR were expanded up to $R_{MT} \times K_{max} = 7.0$ and inside the atomic spheres for the basis wave function. The maximum value of l was taken as $l_{max} = 10$, while the charge density was Fourier expanded up to $G_{max} = 12.0$ $(a.u)^{-1}$. Self-consistency was obtained using 300 $\vec{k}$ points in the irreducible Brillouin zone (IBZ). The self-consistent calculations converged since the total energy of the system is stable within 0.00001 R_y. The electronic band structure calculations were performed within 800 $\vec{k}$ points in the IBZ, and the optical properties calculations were performed within 1500 $\vec{k}$ points in the IBZ.

4. Results and discussion

4.1. Electronic band structure, density of states and valence electronic charge density

In order to explore and exploit the influence of the substitution of Se by Te, the electronic band structures of the two titled compounds were calculated and are illustrated in Fig. 2(a) and (b). It was found that both compounds exhibit direct band gaps of about 0.32 eV and 0.18 eV, which are in good agreement with the measured values of 0.34 eV and 0.19 eV obtained from UV-VIS diffuse reflectance spectroscopy. This fact allows us to neglect spin–orbit interactions for further calculation. It is clear that there is a band gap reduction when we move from Se to Te, which confirms the fact that the mBJ gives good agreement with the experimentally evaluated energy band gap.[29–31] The conduction band minimum (CBM) and the valence band maximum (VBM) of Tl_4PbSe_3 and Tl_4PbTe_3 are located at the Γ point of the first BZ. We set the zero-point of energy (Fermi level) at the VBM. To carefully investigate the electronic structure and the role of the orbitals of each atom in both

Table 1 Atomic coordinates for Tl_4PbSe_3 (SG *P*4/*ncc* (130); $a = 8.5346$ (2), $c = 12.6871$ (7) Å)[26] along with the optimized coordinates obtained by using PBE–GGA

Atom	Wyckoff	*x*/*a*	*x*/*a* (opt.)	*y*/*b*	*y*/*b* (opt.)	*z*/*c*	*z*/*b* (opt.)
Tl	16g	0.12639 (9)	0.13210	0.57852 (9)	0.56987	0.09574 (5)	0.08998
Pb	4c	1/4	1/4	1/4	1/4	0.28456 (11)	0.27997
Se1	4c	1/4	1/4	1/4	1/4	0.0223 (3)	0.02312
Se2	8f	0.4149 (2)	0.40236	0.5851 (2)	0.5987	1/4	1/4

compounds, the angular momentum projected density of states was investigated. Fig. 3(a) illustrates the density of states of Tl_4PbSe_3 and Tl_4PbTe_3, which confirms the occurrence of the increase in magnitude of the band gap.

The angular momentum character of the various structures for Tl_4PbSe_3 and Tl_4PbTe_3 single crystals can be obtained from calculating the angular momentum projected density of states (PDOS) as shown in Fig. 3(b)–(i). The sharp structure between −13.0 and −10.0 eV is mainly formed by the Tl-d, Se1, 2-s and Te1, 2-s states. The structure around 9.0 eV originates from the Pb-s state. The confined structure between −8.0 and −4.0 eV is caused by the Tl-s state. The spectral structure from −4.0 eV up to the Fermi level is formed by the Tl-s/p, Pb-p, Se1, 2-p and Te1, 2-p states. The structure from the CBM and above present an admixture of the Tl-s/p/f, Pb-p/d/f, Se1, 2-p and Te1, 2-p states. We have used the calculated angular momentum decomposition of the atoms projected electronic density of states to elucidate the character of chemical bonding. In the energy region extended between −9.0 eV and the Fermi level (E_F) we obtained a total number of electrons/eV (e/eV) for the orbitals in each atom of the Tl_4PbSe_3 (Tl_4PbTe_3) compounds as follows: Pb-s state 1.9 (1.6) e/eV, Se2-p state 1.8 e/eV, Se1-p state 1.8 e/eV, Te2-p state 1.2 e/eV, Te1-p state 1.3 e/eV, Tl-s state 0.7 (0.6) e/eV, Pb-p state 0.3 (0.3) e/eV, Tl-p state 0.1 (0.1) e/eV and Pb-d state 0.03 (0.03) e/eV. From the contributions of these orbitals to the valence bands, one can see that there are some electrons from Pb, Se, Te and Tl atoms which are transferred into valence bands and contribute in covalent interactions between the atoms. The strength/weakness of the covalent bond arises due to the degree of the hybridization and electronegativity differences between the atoms. It is clear that there is a weak interaction of charges between the atoms due to the existence of weak hybridization, confirming that a weak covalent bonding exists between these atoms. Thus, the angular momentum decomposition of the atoms projected electronic density of states allows us to analyze the nature of the bonds following classical chemical concepts. This concept is very useful to classify compounds into different categories with respect to their different chemical and physical properties.

In order to gain further understanding of the bonding features, we have calculated the charge density distributions in two crystallographic planes, as shown in Fig. 4(a)–(c). This can give a clear image of the electronic charge surrounding the atoms and the principal charge transfer which can help to identify the bonding features. The crystallographic plane in the (100) direction confirms that all atoms are surrounded by a uniform spherical charge forming strong ionic bonding and weak covalent bonds. In addition, we have calculated the crystallographic plane in the direction (101) which confirms our previous observation that the characters of the bonds are strongly ionic and very weakly covalent. We have calculated the bond lengths, as shown in Fig. 1(h)–(j) for Tl_4PbTe_3 and in Table 3 for Tl_4PbSe_3, and in comparison with the measured values, a good agreement was found. The good agreement with the experimental data reveals the accuracy of the method used here.

4.2. Optical response

The calculations of the dielectric functions involve the energy eigenvalues and electron wave functions. These are natural outputs of the band structure calculations. We have performed calculations of the imaginary part of the inter-band frequency dependent dielectric function using the expression[32]

$$\varepsilon_2{}^{ij}(\omega) = \frac{8\pi^2\hbar^2e^2}{m^2V}\sum_k\sum_{cv}(f_c - f_v)\frac{p_{cv}{}^i(k)p_{vc}{}^j(k)}{E_{vc}{}^2}\,\delta[E_c(k) - E_v(k) - \hbar\omega] \quad (1)$$

where m, e and $\hbar$ are the electron mass, charge and Planck's constant, respectively. f_c and f_v represent the carrier Fermi distributions for the conduction and valence bands, respectively. The term $p_{cv}{}^i(k)$ denotes the momentum matrix element transition from the energy level c of the conduction band to the level v of the valence band at a certain k-point in the BZ, and V is

Table 2 Atomic coordinates for Tl_4PbTe_3 (SG *I*4/*mcm* (140); $a = 8.841$, $c = 13.056$ Å)[27] along with the optimized coordinates obtained by using PBE–GGA

Atom	Wyckoff	*x*/*a*	*x*/*a* (opt.)	*y*/*b*	*y*/*b* (opt.)	*z*/*c*	*z*/*b* (opt.)
Tl	16l	0.1461	0.1501	0.6461	0.6598	0.1594	0.1610
Pb	4c	0	0	0	0	0	0
Te1	4a	0	0	0	0	1/4	1/4
Te2	8h	0.6623	0.6543	0.1623	0.1601	0	0

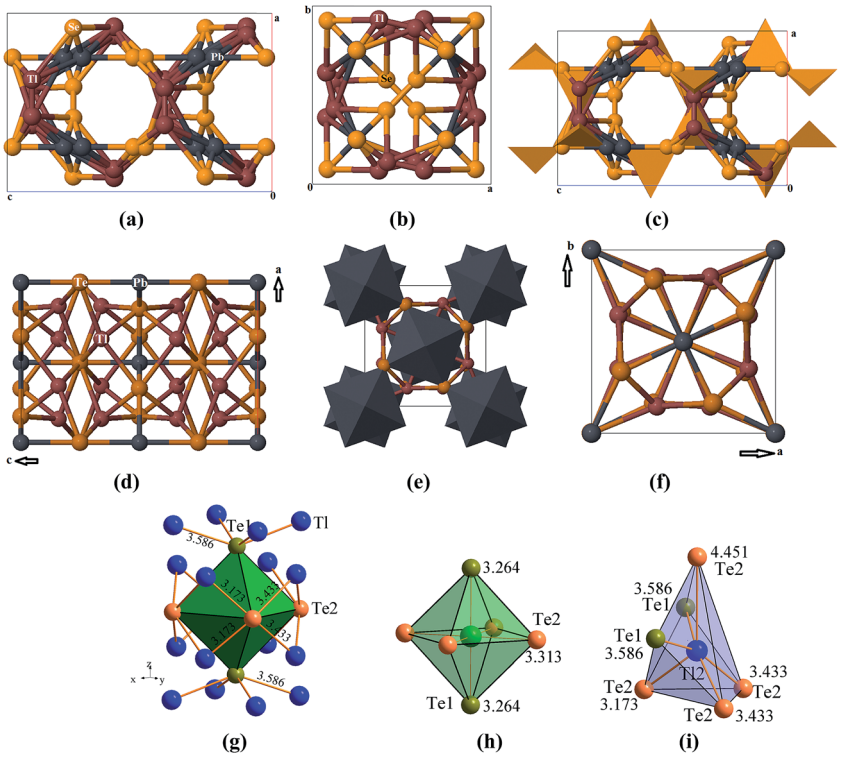

Fig. 1 The crystalline structures; (a–c) Tl_4PbSe_3 (space group *P*4/*ncc* (130); lattice constants $a = 8.5346$ (2), $c = 12.6871$ (7) Å)[26]; (d–i) Tl_4PbTe_3 (space group *I*4/*mcm* (140); $a = 8.841$, $c = 13.056$ Å)[27]; (g–i) show the bond lengths of Tl_4PbTe_3.

the unit cell volume. The linear optical properties were calculated using the optical code implemented in the WIEN2k package,[19] for more details please see the user guide[33] and ref. 32.

The real parts $\varepsilon_1^{II}(\omega)$ and $\varepsilon_1^{\perp}(\omega)$ can be obtained using the Kramers–Kronig relations.[32]

$$\varepsilon_1(\omega) = 1 + \frac{2}{\pi} P \int_0^{\infty} \frac{\omega' \varepsilon_2(\omega')}{\omega'^2 - \omega^2} d\omega' \quad (2)$$

where *P* implies the principal value of the integral.

We should emphasize that the optical properties can provide detailed information about the electronic structure of the

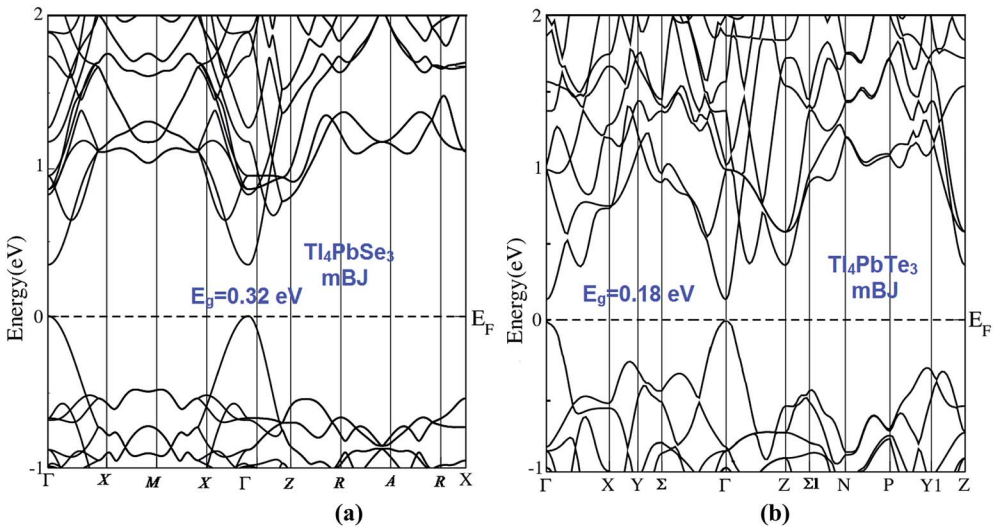

Fig. 2 Calculated electronic band structure using mBJ for; (a) Tl_4PbSe_3, which exhibits a direct band gap of about 0.32 eV, which is in good agreement with the measured value of 0.34 eV obtained from UV-VIS diffuse reflectance spectroscopy; (b) Tl_4PbTe_3, which exhibits a direct band gap of about 0.18 eV, which is in good agreement with the measured value of 0.19 eV obtained from UV-VIS diffuse reflectance spectroscopy.

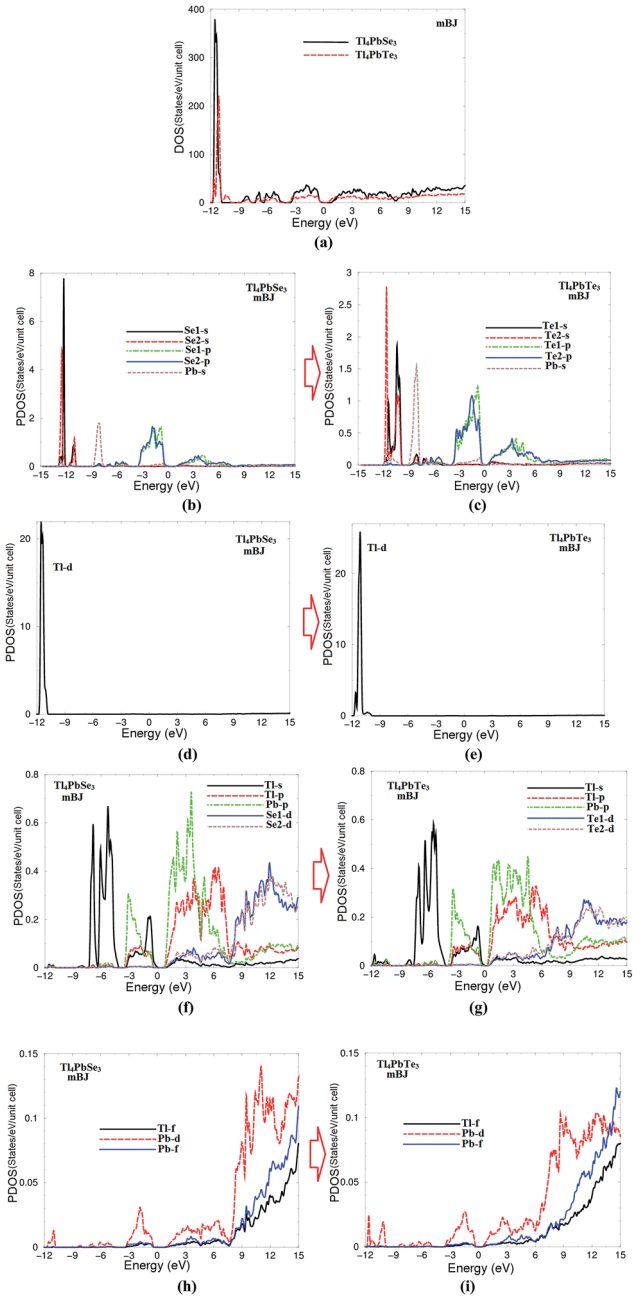

Fig. 3 Calculated density of states (states/eV unit cell) using mBJ; (a) density of states for Tl_4PbSe_3 and Tl_4PbTe_3; (b) calculated Se1, 2-s/p and Pb-s partial density of states for Tl_4PbSe_3; (c) calculated Te1, 2-s/p and Pb-s partial density of states for Tl_4PbTe_3; (d) calculated Tl-d partial density of states for Tl_4PbSe_3; (e) calculated Tl-d partial density of states for Tl_4PbTe_3; (f) calculated Tl-s/p, Pb-p and Se1, 2-d partial density of states for Tl_4PbSe_3; (g) calculated Tl-s/p, Pb-p and Te1, 2-d partial density of states for Tl_4PbTe_3; (h) calculated Tl-f and Pb-d/f partial density of states for Tl_4PbSe_3; (i) calculated Tl-f and Pb-d/f partial density of states for Tl_4PbTe_3.

materials. Therefore, we have calculated the imaginary and real part dispersions using the above mentioned expressions. The principal optical components are determined by inter-band transitions from the valence into the conduction bands. According to the dipolar selection rule, only transitions changing the angular momentum quantum number l by unity ($\Delta = \pm 1$) are allowed.

In Fig. 5(a) and (b), we illustrate the dispersions of the imaginary part of the optical components $\varepsilon_2^{\perp}(\omega)$ and $\varepsilon_2^{\mathrm{II}}(\omega)$, along with the real parts $\varepsilon_1^{\perp}(\omega)$ and $\varepsilon_1^{\mathrm{II}}(\omega)$ for the Tl_4PbSe_3 and Tl_4PbTe_3 compounds, calculated using the mBJ approach.

It is clear that the substitution of Se by Te causes the whole spectral structure to shift towards lower energies with an increase in the magnitude of the spectral structures. The confirmation of the reduction in the energy gap when we move from Se to Te is in good agreement with our observation from the electronic band structure and the density of states. The first critical points (absorption edges) are located at 0.32 eV and 0.18 eV for Tl_4PbSe_3 and Tl_4PbTe_3. It has been noticed that both compounds exhibit one main spectral peak, which is situated at around 3.0 eV for Tl_4PbSe_3 while it is located at around 2.0 eV for Tl_4PbTe_3. Beyond the main peak, a prompt reduction occurs when we increase the photon energy. The strength of the main peaks could be explained by the fact that $\varepsilon_2(\omega)$ scales as $1/\omega^2$.

The observed structures in $\varepsilon_2(\omega)$ are caused by optical transitions from the valence bands to the conduction bands, which can be analyzed using the calculated electronic band structure. The absorption edges and the main peak occurs due to the optical transitions between Se1/Se2-p, (Te1/Te2-p), Pb-s/p/d, Tl-s/p and Se1/Se2-p, (Te1/Te2-p), Te1/Te2-d, Pb-p/d, Se1/Se2-d, (Te1/Te2-d) according to the optical selection rules.

To support the theoretical calculations, we have measured the dispersions of the imaginary part of the dielectric susceptibility $\varepsilon_2(\omega)$ for Tl_4PbSe_3 and Tl_4PbTe_3 single crystals, as shown in Fig. 5(c). From the measured $\varepsilon_2(\omega)$, we have evaluated the experimental optical band gaps which are equal to 0.34 eV (Tl_4PbSe_3) and 0.19 eV (Tl_4PbTe_3). This confirms our observation from the theoretical calculations that the substitution of Se by Te causes a band gap reduction, resulting in a shift of the optical spectra towards lower energies, which is as predicted by calculations. Therefore, our calculated $\varepsilon_2(\omega)$ succeeds in bringing the above features into close agreement with the measured ones, which confirms the accuracy of the theoretical calculations.

From the calculated real parts (Fig. 5(a) and (b)), we have obtained the vanishing frequency value of the dielectric function, which defines the static electronic dielectric constant $\varepsilon_1^{\perp}(0)$ and $\varepsilon_1^{\mathrm{II}}(0)$. It is clear that the two optical components exhibit isotropic behavior, which is confirmed by the calculated values of the uniaxial anisotropy $\delta\varepsilon = [(\varepsilon_0^{\mathrm{II}} - \varepsilon_0^{\perp})/\varepsilon_0^{\mathrm{tot}}]$. These values, along with $\varepsilon_1^{\perp}(0)$, $\varepsilon_1^{\mathrm{II}}(0)$ and $\varepsilon_1^{\mathrm{tot}}(0)$, are listed in Table 4. Following Table 4 we can see that these materials exhibit negative uniaxial anisotropy. Using the calculated values of $\varepsilon_1^{\perp}(0)$, $\varepsilon_1^{\mathrm{II}}(0)$, $\omega_{\mathrm{p}}^{\perp}(\omega)$ and $\omega_{\mathrm{p}}^{\mathrm{II}}(\omega)$ we can estimate the energy gap value based on the Penn model.[34] Penn proposed a relation between $\varepsilon(0)$ and E_g, $\varepsilon(0) \approx 1 + (\hbar\omega_{\mathrm{p}}/E_g)^2$, where E_g is some kind of averaged energy gap, which could be related to the real energy gap. Thus, the larger $\varepsilon_1(0)$ value corresponds to the small energy gap. This is further evidence that moving from Se to Te causes a reduction in band gap. We would like to mention that $\omega_{\mathrm{p}}^{\perp}(\omega)$ and $\omega_{\mathrm{p}}^{\mathrm{II}}(\omega)$ are very important features in the optical spectrum. These are the plasmon oscillations which occur at energies

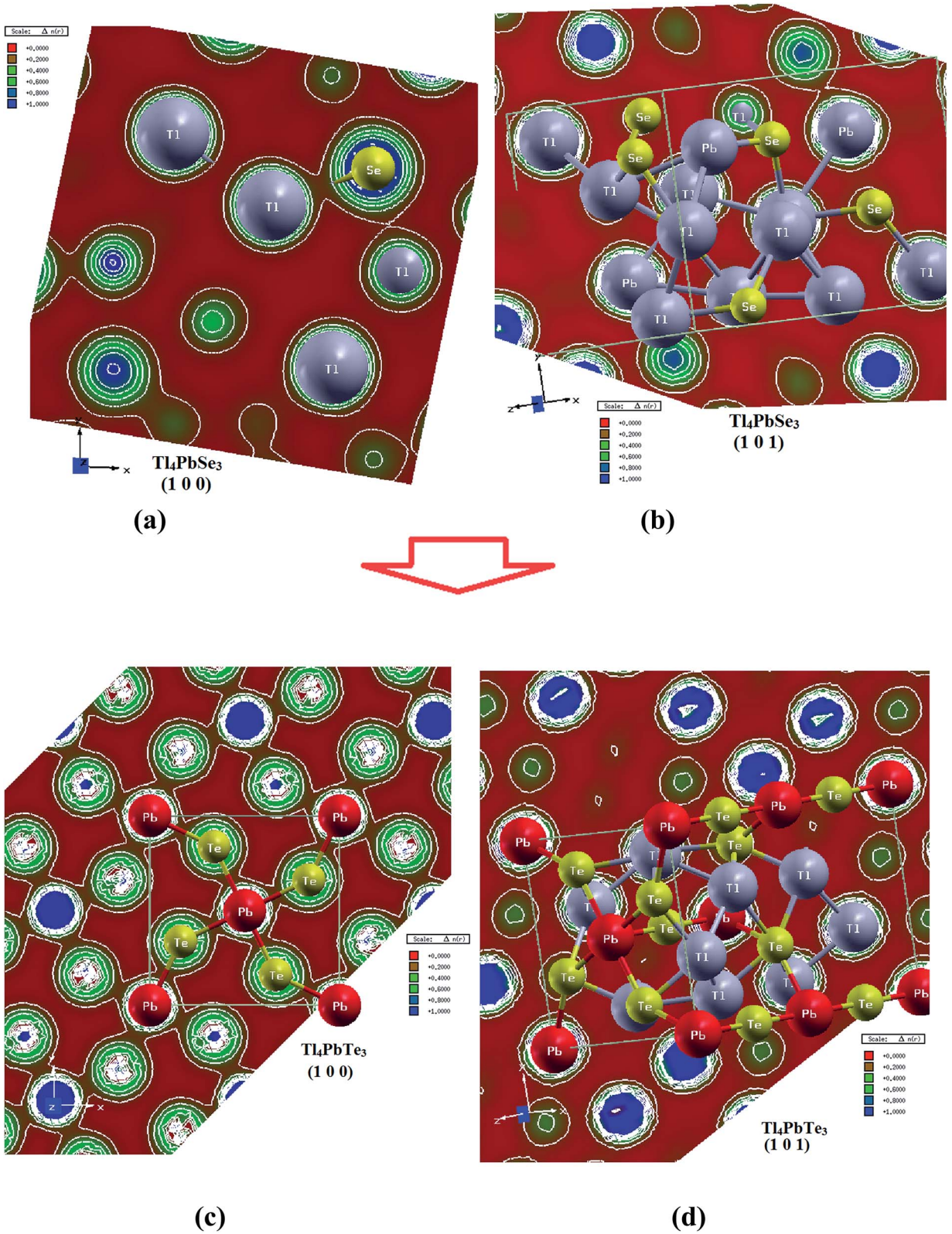

Fig. 4 Calculated electronic charge density distribution for two crystallographic planes using mBJ; (a) the (100) crystallographic plane of Tl_4PbSe_3; (b) the (101) crystallographic plane of Tl_4PbSe_3; (c) the (100) crystallographic plane of Tl_4PbTe_3; (d) the (101) crystallographic plane of Tl_4PbTe_3.

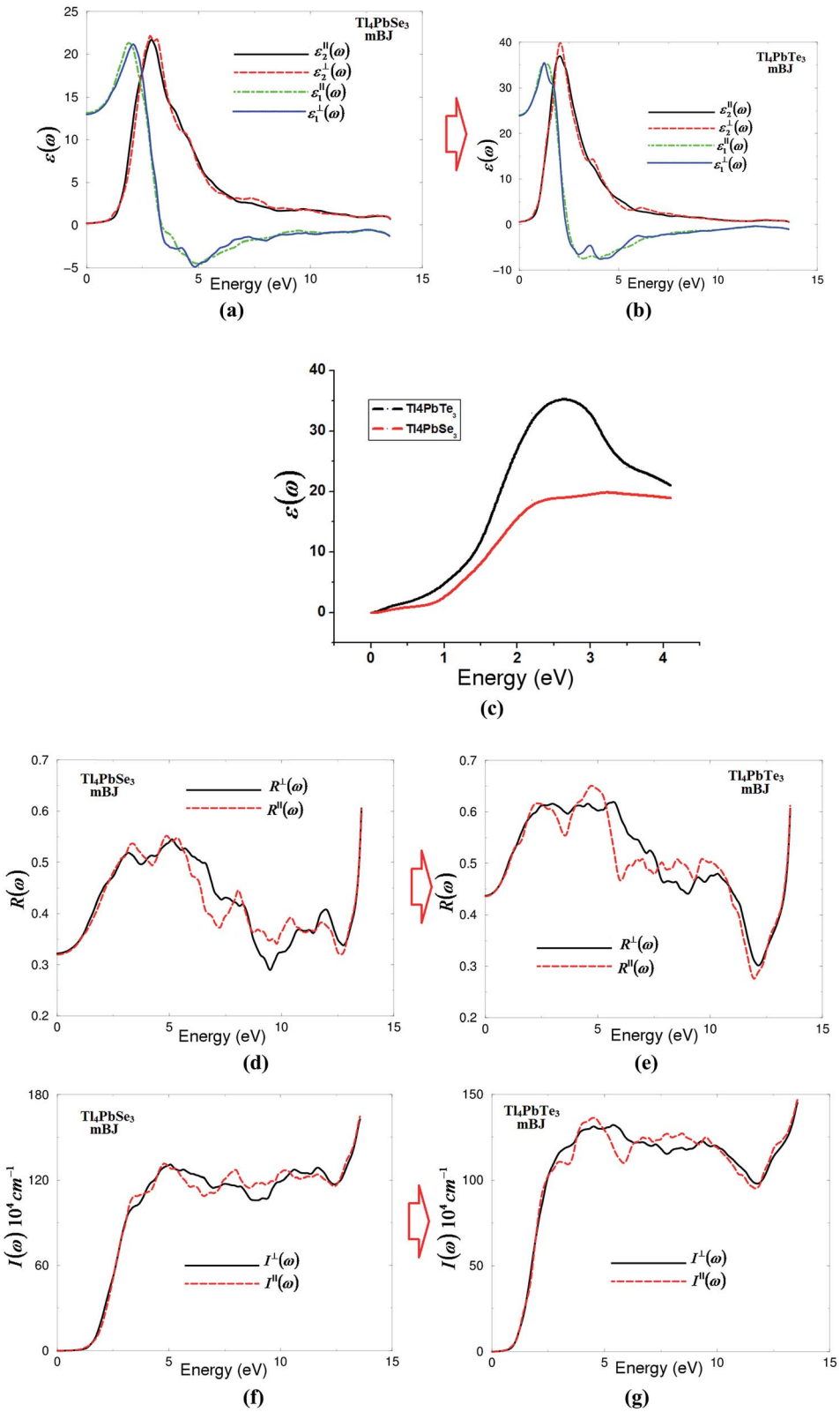

Fig. 5 (a) Calculated $\varepsilon_2^{\perp}(\omega)$ dispersion (black solid curve), $\varepsilon_2^{\parallel}(\omega)$ (red dashed curve) along with calculated $\varepsilon_1^{\perp}(\omega)$ (green dotted dashed curve), $\varepsilon_1^{\parallel}(\omega)$ (blue light dotted curve) for the Tl_4PbSe_3 compound using mBJ; (b) calculated $\varepsilon_2^{\perp}(\omega)$ dispersion (black solid curve), $\varepsilon_1^{\parallel}(\omega)$ (red dashed curve) along with calculated $\varepsilon_2^{\perp}(\omega)$ (green dotted dashed curve), $\varepsilon_1^{\parallel}(\omega)$ (blue dotted curve) for the Tl_4PbTe_3 compound using mBJ; (c) the measured imaginary part of the dielectric susceptibility for Tl_4PbSe_3 and Tl_4PbSe_3; (d) calculated $R^{\perp}(\omega)$ (black solid curve), $R^{\parallel}(\omega)$ (red dashed curve) for the Tl_4PbSe_3 compound using mBJ; (e) calculated $R^{\perp}(\omega)$ (black solid curve), $R^{\parallel}(\omega)$ (red dashed curve) for the Tl_4PbTe_3 compound using mBJ. (f) Calculated $I^{\perp}(\omega)$ (black solid curve), $I^{\parallel}(\omega)$ (red dashed curve) for the Tl_4PbSe_3 compound using mBJ; (g) calculated $I^{\perp}(\omega)$ (black solid curve), $I^{\parallel}(\omega)$ (red dashed curve) for the Tl_4PbTe_3 compound using mBJ.

Table 3 Calculated bond lengths of Tl_4PbSe_3 in comparison with the experimental data[26]

Bond	Bond lengths (Å) exp.	Bond lengths (Å) this work	Bond	Bond lengths (Å) exp.	Bond lengths (Å) this work
Tl1–Se4	3.0064	3.1005	Se3–Pb2	3.0162	3.0001
Tl1–Se3	3.1372	3.1011	Se3–Tl1	3.1372	3.1299
Tl1–Se4	3.1459	3.1321	Se3–Tl1	3.1372	3.1299
Tl1–Se4	3.4923	3.5011	Se3–Tl1	3.1372	3.1299
Tl1–Tl1	3.5146	3.4901	Se3–Tl1	3.1372	3.1299
Tl1–Tl1	3.5230	3.5012	Se3–Pb2	3.3273	3.3199
Tl1–Tl1	3.5230	3.5099	Se4–Tl1	3.0064	3.0001
Tl1–Tl1	3.6082	3.5999	Se4–Tl1	3.0064	3.0001
Pb2–Se3	3.0162	3.0290	Se4–Tl1	3.1459	3.1501
Pb2–Se4	3.2175	3.2011	Se4–Tl1	3.1459	3.1501
Pb2–Se4	3.2175	3.2011	Se4–Pb2	3.2175	3.2099
Pb2–Se4	3.2175	3.2011	Se4–Pb2	3.2175	3.2099
Pb2–Se4	3.2175	3.2011	Se4–Tl1	3.4923	3.5000
Pb2–Se3	3.3273	3.3199	Se4–Tl1	3.4923	3.5000

Table 4 The calculated energy band gaps in comparison with experimental values, $\varepsilon_1^{\perp}(0)$, $\varepsilon_1^{\parallel}(0)$, $\delta\varepsilon$, $\omega_p^{\perp}(\omega)$ and $\omega_p^{\parallel}(\omega)$ for Tl_4PbSe_3 and Tl_4PbTe_3 using PBE–GGA and mBJ

	Tl_4PbSe_3		Tl_4PbTe_3	
	PBE–GGA	mBJ	PBE–GGA	mBJ
Eg (eV)	0.21	0.32	0.10	0.18
$\varepsilon_1^{\perp}(0)$	14.23	13.16	25.11	24.07
$\varepsilon_1^{\mathrm{II}}(0)$	13.87	12.99	24.32	23.93
$\delta\varepsilon$	−0.012	−0.012	−0.015	−0.002
$\omega_p^{\perp}(\omega)$	3.11	3.38	2.10	2.46
$\omega_p^{\mathrm{II}}(\omega)$	3.01	3.33	2.02	2.35

where $\varepsilon_1(\omega)$ crosses zero, and they are associated with the existence of plasma oscillations (plasmons).

For more details, we also calculated other optical properties, such as the reflectivity spectra and the absorption coefficients. Fig. 5(d) and (e) show the calculated $R^{\perp}(\omega)$ and $R^{\mathrm{II}}(\omega)$ of the Tl_4PbSe_3 and Tl_4PbTe_3 compounds. It has been found that in the low energy region (below 1.0 eV), Tl_4PbSe_3 exhibits lower reflectivity than the Tl_4PbTe_3 compound. Increasing the photon energy leads to an increase in the reflectivity up to 55% (Tl_4PbSe_3) and 65% (Tl_4PbTe_3). The first reflectivity maxima occur at around 3.48 and 3.33 for $R^{\perp}(\omega)$ and $R^{\mathrm{II}}(\omega)$ of Tl_4PbSe_3, whereas they occur at 2.46 and 2.35 for $R^{\perp}(\omega)$ and $R^{\mathrm{II}}(\omega)$ of Tl_4PbTe_3. These are the values of $\omega_p^{\perp}(\omega)$ and $\omega_p^{\mathrm{II}}(\omega)$ which confirm the occurrences of the plasmon resonance. The first reflectivity minima occurs at around 9.0 eV (Tl_4PbSe_3) and 12.0 eV (Tl_4PbTe_3). The absorption coefficient features of the Tl_4PbSe_3 and Tl_4PbTe_3 compounds are illustrated in Fig. 5(f) and (g). The figures show the fundamental optical absorption edges situated at 0.32 eV (Tl_4PbSe_3) and 0.18 eV (Tl_4PbTe_3), matching the experimental values of the absorption edges (0.34 eV and 0.19 eV). Rapid increases occur after the absorption edges to reach the maximum absorption at around 5.0 eV (Tl_4PbSe_3) and 4.0 eV (Tl_4PbTe_3). It is clear that the Tl_4PbSe_3 and Tl_4PbTe_3 compounds possess a relatively wide optical transparency region, up to 0.32 eV ($\lambda = 38\,750$ Å) for Tl_4PbSe_3 and 0.18 eV ($\lambda = 68\,888$ Å) for Tl_4PbTe_3, which is in good agreement with the experimental data (0.34 and 0.19 eV).

5. Conclusions

We have reported comprehensive theoretical calculations for Tl_4PbSe_3 and Tl_4PbTe_3 single crystals using the full potential method within PBE–GGA and mBJ approaches. The experimental crystal structures were optimized by minimizing the forces acting on the atoms using the PBE–GGA approach. The calculated electronic band structure reveals that these compounds possess direct energy band gaps of about 0.21 eV (PBE–GGA) and 0.32 eV (mBJ) for Tl_4PbSe_3 in comparison with the experimental values (0.34 eV), while for Tl_4PbTe_3, the band gap values are 0.10 eV (PBE–GGA) and 0.18 eV (mBJ) compared to the experimental one (0.19 eV). We have found that mBJ succeeds by large amount in bringing the calculated gap into close agreement with the measured one. The calculated angular momentum projected density of states showed that strong/weak hybridization exists between the states, revealing the existence of covalent bonding. The calculated bond lengths show good agreement with the measured values. The optical properties gave deep insight into the electronic structures and show that these materials exhibit negative uniaxial anisotropy. We have measured the dispersions of the imaginary part of the dielectric susceptibilty $\varepsilon_2(\omega)$ for the Tl_4PbSe_3 and Tl_4PbTe_3 compounds, which helps to evaluate the experimental optical band gaps and confirms our observation from the theoretical calculations that substituting Se by Te causes a band gap reduction, as predicted by calculations. Therefore, our calculated $\varepsilon_2(\omega)$ succeeds by a large amount in bringing the above features into close agreement with the measured ones, revealing the accuracy of the theoretical calculations.

Acknowledgements

The result was developed within the CENTEM project, reg. no. CZ.1.05/2.1.00/03.0088, co-funded by the ERDF as part of the Ministry of Education, Youth and Sports OP RDI programme

and, in the follow-up sustainability stage, supported through CENTEM PLUS (LO1402) by financial means from the Ministry of Education, Youth and Sports under the National Sustainability Programme I. Computational resources were provided by MetaCentrum (LM2010005) and CERIT-SC (CZ.1.05/3.2.00/08.0144) infrastructures.

References

1 L. Z. Kelley, I. Mandel and E. Ramirez-Ruiz, *Phys. Rev. D: Part., Fields, Gravitation, Cosmol.*, 2013, **87**, 123004.
2 H. Wang, A. Charoenphakdee, K. Kurosaki, S. Yamanaka and G. Jeffrey Snyder, *Phys. Rev. B: Condens. Matter Mater. Phys.*, 2011, **83**, 024303.
3 A. Kosuga, K. Kurosaki, H. Muta and S. Yamanaka, *J. Appl. Phys.*, 2006, **99**, 063705.
4 B. A. Kuropatwa, A. Assoud and H. Kleinke, *J. Alloys Compd.*, 2011, **509**, 6768–6772.
5 A. Kosuga, K. Kurosaki, H. Muta and S. Yamanaka, *J. Appl. Phys.*, 2006, **99**, 063705.
6 A. L. Ajavon, R. Eholie, Y. Piffard and M. Tournoux, *Rev. Chim. Miner.*, 1983, **20**, 421–425.
7 A. Ibanez, J. C. Jumas, E. Philippot, A. L. Ajavo and R. Eholie, *Rev. Chim. Miner.*, 1986, **23**, 281–289.
8 T. A. Malakhovskaya-Rosokha, M. Yu. Sabov, I. E. Barchiy and E. Yu. Peresh, *Russ. J. Inorg. Chem.*, 2011, **56**, 118.
9 P. Houenou, R. Eholie and J. Flahaut, *C. R. Seances Acad. Sci., Ser. C*, 1979, **283**, 193–195.
10 P. Houenou, R. Eholie and J. Flahaut, *J. Less-Common Met.*, 1981, **81**, 181–197.
11 P. Houenou, A. L. Ajavon and G. A. Fatseas, *C. R. Seances Acad. Sci., Vie Acad.*, 1982, **295**(4), 455–457.
12 E. Dichi, G. Kra, R. Eholie and B. Legendre, *J. Alloys Compd.*, 1993, **194**, 155–161.
13 E. Dichi, G. Kra, R. Eholie and B. Legendre, *J. Alloys Compd.*, 1993, **199**, 7–19.
14 E. Dichi, G. Kra, R. Eholie and B. Legendre, *J. Alloys Compd.*, 1993, **199**, 21–46.
15 S. Bucchia, C. Jumas, E. Philippot and M. Maurin, *Rev. Chim. Miner.*, 1981, **18**, 224–234.
16 S. Bradtmöller, R. K. Kremer and P. Böttcher, *Z. Anorg. Allg. Chem.*, 1994, **620**, 1073–1080.
17 S. Bradtmöller and P. Böttcher, *Z. Anorg. Allg. Chem.*, 1993, **619**, 1155–1160.
18 M. I. Kolinko, I. V. Kityk and A. S. Krochuk, *J. Phys. Chem. Solids*, 1992, **53**, 1315–1320.
19 P. Blaha, K. Schwarz, G. K. H. Madsen, D. Kvasnicka and J. Luitz, WIEN2k, *An augmented plane wave plus local orbitals program for calculating crystal properties*, Vienna University of Technology, Austria, 2001.
20 F. Tran and P. Blaha, *Phys. Rev. Lett.*, 2009, **102**, 226401.
21 A. H. Reshak and S. Azam, *Opt. Mater.*, 2014, **37**, 97–103.
22 A. H. Reshak and S. Auluck, *Opt. Mater.*, 2014, **38**, 80–86.
23 A. H. Reshak, S. A. Khan and Z. A. Alahmed, *Opt. Mater.*, 2014, **37**, 322–326.
24 A. H. Reshak, *Opt. Mater.*, 2015, **46**, 216–222, DOI: 10.1016/j.optmat.2015.04.022.
25 H. S. Saini, M. Singh, A. H. Reshak and M. K. Kashyap, *J. Magn. Magn. Mater.*, 2013, **331**, 1–6.
26 T. O. Malakhovska, M. Yu. Sabov, E. Yu. Peresh, V. Pavlyuk and B. Marciniak, *Chemistry of Metals and Alloys*, 2009, **2**, 15–17.
27 S. Bradtmöller and P. Böttcher, *Z. Anorg. Allg. Chem.*, 1993, **619**, 1155–1160.
28 J. P. Perdew, S. Burke and M. Ernzerhof, *Phys. Rev. Lett.*, 1996, **77**, 3865.
29 A. H. Reshak, H. Kamarudin and S. Auluck, *J. Mater. Sci.*, 2013, **48**, 1955–1965.
30 A. H. Reshak, I. V. Kityk, O. V. Parasyuk, A. O. Fedorchuk, Z. A. Alahmed, N. AlZayed, H. Kamarudin and S. Auluck, *J. Mater. Sci.*, 2013, **48**, 1342–1350.
31 A. H. Reshak, I. V. Kityk, O. V. Parasyuk, H. Kamarudin and S. Auluck, *J. Phys. Chem. B*, 2013, **117**, 2545–2553.
32 C. Ambrosch-Draxl and J. O. Sofo, *Comput. Phys. Commun.*, 2006, **175**, 1–14.
33 http://www.wien2k.at/reg_user/textbooks/usersguide.pdf.
34 D. R. Penn, *Phys. Rev. B: Condens. Matter Mater. Phys.*, 1962, **128**, 2093.